Coronary Artery Flow Modeling in an Ex-vivo Biorobotic Heart*

Manisha Singh, Julia Situ, Carly Long, Diego Quevedo-Moreno, Ginger Schmidt, Néstor Uribe-Patarroyo, Ellen T. Roche, *Member, IEEE*

2025 IEEE 8th International Conference on Soft Robotics (RoboSoft) | 979-8-3315-2020-5/25/$31.00 ©2025 IEEE | DOI: 10.1109/RoboSoft63089.2025.11020957

*Research supported by NIH R01 grant to N.U-P.

M.S. is with the Institute for Medical Engineering and Science at the Massachusetts Institute of Technology, Cambridge, MA 02139 (e-mail: smanisha@mit.edu).

J.S. was with the Department of Electrical Engineering and Computer Science at the Massachusetts Institute of Technology, Cambridge, MA 02139 (email: jsitu@mit.edu).

C.L. is with the Department of Mechanical Engineering at the Massachusetts Institute of Technology, Cambridge, MA 02139 (email: carlylo@mit.edu).

D.Q.M is with the Department of Mechanical Engineering at the Massachusetts Institute of Technology, Cambridge, MA 02139 (email: dquevedo@mit.edu).

G.S. is with the Wellman Center for Photomedicine, Harvard Medical School and Massachusetts General Hospital, 40 Blossom Street, Boston, Massachusetts 02114, USA, and the Institute for Medical Engineering and Science, Massachusetts Institute of Technology, Cambridge, 77 Massachusetts Avenue, Massachusetts 02139, USA (email: gingers@mit.edu).

N.U-P. is with the Wellman Center for Photomedicine at the Harvard Medical School and Massachusetts General Hospital, 40 Blossom Street, Boston, Massachusetts 02114, USA (corresponding author, email: uribepatarroyo.nestor@mgh.harvard.edu).

E. T. R. is with the Department of Mechanical Engineering and the Institute for Medical Engineering and Science at the Massachusetts Institute of Technology, Cambridge, MA 02139 (corresponding author, e-mail: etr@mit.edu).

***Abstract*— Coronary artery disease remains a significant global health concern, leading to high morbidity and mortality, with conditions like spontaneous coronary artery dissection (SCAD) presenting unique challenges in diagnosis and treatment. SCAD, a critical cause of acute coronary syndrome and myocardial infarction, complicates percutaneous coronary intervention (PCI) due to the fragility of the affected vessels. To improve PCI techniques specifically tailored to treat SCAD, we developed an ex-vivo biorobotic coronary artery flow simulator to model SCAD in a benchtop setup. The simulator integrates intraventricular balloons, McKibben soft robotic actuators, and a synchronized flow loop to replicate physiological coronary flow and myocardial wall motion in an explanted porcine heart. After recreating healthy conditions of ventricular wall motion and coronary flow, we induced a coronary dissection model, performed stent implantation, and assessed the intervention deployment using intravascular optical coherence tomography (IV-OCT). This platform can potentially enable precise testing of interventional strategies, improve PCI techniques, examine catheter or PCI-induced dissection, train clinicians, and facilitate testing of novel coronary imaging and intervention devices.**

I. INTRODUCTION

Coronary artery disease remains a leading cause of death globally, with myocardial infarction being one of its most severe manifestations [1]. Spontaneous coronary artery dissection (SCAD) has gained recognition as a critical, yet frequently underdiagnosed, cause of acute coronary syndrome and myocardial infarction, particularly among patients who do not present with conventional atherosclerotic risk factors [2]. Proper diagnosis of SCAD is crucial because its treatment approach differs significantly from standard protocols used for atherosclerotic acute coronary syndrome [2-4]. Misdiagnosis or inappropriate treatment can lead to worse patient outcomes [3].

Treating SCAD with percutaneous coronary intervention (PCI) carries a higher risk of complications, such as iatrogenic dissections, compared to PCI for atherosclerotic disease [5, 6]. These risks arise from the structural fragility of SCAD-affected arteries due to disruptions in the arterial wall and intramural hematoma formation. Such factors reduce the vessel's mechanical integrity, making it more prone to injury during interventions [3, 7]. The challenges in treating SCAD highlight the need for advanced models to test, refine, and optimize PCI techniques specific to SCAD patients. Current animal models, though valuable, are expensive and complex to manage [8]. 3D-printed models can replicate the anatomical structures but often fail to replicate the dynamic mechanical properties, including Young's modulus, of native coronary vasculature, which is crucial for simulating SCAD [9, 10]. Moreover, existing cardiac simulators are limited in their ability to accurately mimic myocardial wall motion—expansion during diastole and contraction during systole—since they rely on external pumps to drive wall motion. Soft robotic simulators have emerged as a promising alternative, offering biomimetic deformation capabilities through pneumatic and fluidic actuation strategies. Several state-of-the-art approaches have been developed to model cardiovascular disease and intervention, including both 3D-printed and biohybrid simulators. For instance, our 3D-printed cardiac simulator integrates soft robotic sleeves externally mounted on the ventricular wall to mimic aortic stenosis lesions and associated diastolic dysfunction, enabling precise replication of hemodynamic parameters for testing prosthetic aortic valves [11]. While these models offer high-fidelity anatomical reconstruction and hemodynamic control, they lack the compliant mechanical properties necessary to mimic dynamic vascular behavior, particularly for coronary flow studies. In contrast, biohybrid heart simulators, which integrate explanted myocardial tissue with soft robotic actuation, provide a tunable and controllable platform that preserves both anatomical and mechanical fidelity [12, 13]. However, to achieve effective pumping in these biohybrid models, partial removal of the native myocardial muscle is often required to accommodate soft robotic actuators. Both 3D-printed and biohybrid heart simulators rely on externally integrated soft robotic actuators mounted on the outer myocardial wall. While this design is well-suited for recreating global myocardial motion, it poses a significant limitation for coronary flow modeling. The contraction of externally mounted actuators can inadvertently compress the coronary vasculature, altering flow dynamics and making it difficult to study delicate interventions such as PCI for SCAD. Partial removal of native myocardial muscle also disrupts the natural coronary embedding within the myocardium. Another alternative is perfusion-based working heart models, such as PhysioHeart, which can replicate near-physiological myocardial wall motion but rely on continuous perfusion which significantly increases experimental complexity, and requires specialized perfusates. Furthermore, these models have been primarily focused on electrophysiological assessments [14].

Our simulator seeks to address the limitations of existing models by developing an ex-vivo coronary artery flow simulator that replicates physiological coronary flow and myocardial wall motion in a porcine heart without requiring external myocardial actuation or myocardial tissue removal. Instead, the model achieves circumferential motion (ventricular dilation) using intraventricular balloons, which are placed inside the right and left ventricles and inflated rhythmically to simulate the cardiac cycle. These balloons replicate the circumferential expansion and contraction of the heart muscle during diastole and systole, mimicking physiological heart dynamics. In addition, localized longitudinal myocardial wall motion is replicated using a McKibben soft robotic actuator [15, 16] attached to the outer myocardial wall. This actuator, designed to contract longitudinally in sync with balloon deflation, simulates the natural longitudinal shortening of the heart muscle during contraction.

To demonstrate the model's capability to replicate the environment of a beating heart during PCI and its applicability to testing SCAD treatment strategies, we created a diseased model of SCAD by inducing coronary intimal dissection in a porcine heart. We then treated the dissection by implanting a coronary stent and confirmed the placement of the stent using intravascular optical coherence tomography (IV-OCT) imaging [17, 18]. This ability to induce and repair SCAD lesions within a realistic environment, coupled with high-resolution imaging, showcases the platform’s potential for advancing PCI techniques and optimizing intervention outcomes in SCAD cases.

II. METHODS

A. *Myocardial Actuation and Wall Movement with Intraventricular Balloons*

To prepare the porcine hearts (n=3), frozen hearts were first thawed in distilled water and thoroughly cleaned to remove any remaining blood from the chambers and coronary arteries. Healthy hearts were explanted from pigs according to the Massachusetts Institute of Technology (MIT) Institutional Animal Care and Use Committee (IACUC) protocol number 2311000601, adhering to the National Research Council’s guidelines for the ethical treatment of laboratory animals, or were purchased from Sierra for Medical Science Inc.

To recreate physiologically representative heart motion, specifically ventricular filling during diastole, intraventricular balloons were used. These balloons, purchased from Poba Medical through Chamfr, were a mix of tear-drop-shaped (polyurethane, 28 mL, 35 x 60 mm, PBA17167) and cylindrical-shaped (pellethane 80AE, 46 x 49 mm, PBA23562) designs. Two tear-drop-shaped balloons were placed in the right ventricle (RV) to match the crescent curvature, while one cylindrical-shaped balloon was placed in the left ventricle (LV) to fit its more elliptical shape. The balloons were heat-sealed at the proximal neck to prevent leakage. At the distal neck, they were assembled by securing their tubing to a barbed adapter with a Luer lock, held in place using cyanoacrylate glue (Loctite 422) and zip ties. This assembly was connected to 1/8” inner diameter (ID) and 1/4” outer diameter (OD) firm tubing (McMaster) to facilitate airflow. Additionally, 1/16” ID and 1/8” OD tubing were inserted into each balloon to maintain structural integrity and prevent kinking or folding along the length of the balloon during insertion into the heart chambers (**Fig. 1**).

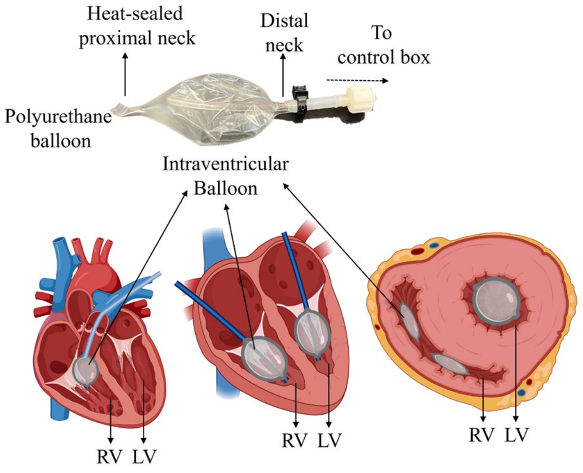

Fig. 1. Assembly and positioning of the intraventricular balloons for ventricular myocardial wall motion.

The balloons were cyclically inflated and deflated pneumatically at pressures of 1–5 psi at 60 beats per minute (bpm) using a custom-built electro-pneumatic control box [19, 20]. Our custom electropneumatic control system uses SMC electropneumatic pressure regulators (ITV1030) and solenoid valves (NVKF333). A microcontroller inputs the desired pressure waveform to the regulator, connected to a wall air supply, and controls the solenoid valve via a 12V MOSFET to actuate the balloons and McKibben actuators. The control box was designed to allow for both inflation and deflation (via vacuum) of the balloons. For testing without vacuum, a fixed pressure of 5 psi was applied to the balloons. To simulate local longitudinal shortening of the myocardial wall, a McKibben [21] soft-robotic actuator was anchored externally to the myocardial wall using a cyanoacrylate-based (Loctite 422) adhesive (**Fig. 2**).

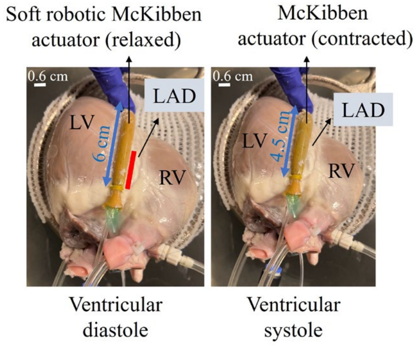

Fig. 2. Soft robotic McKibben actuator in relaxed (diastole, left) and contracted (systole, right) states, anchored to an explanted porcine heart to simulate localized longitudinal myocardial shortening. LV; left ventricle,

RV; right ventricle, LAD; left anterior descending coronary artery. The longitudinal contraction was analyzed in the section shown by the red block.

To quantify myocardial wall motion produced by the intraventricular balloons, M-mode ultrasonography was performed using a Philips Epiq CVx cardiovascular ultrasound system equipped with XL14-3 and X5-1 transducers. M-mode data, capturing the dynamic wall motion, was analyzed and visualized using Q-Vue 2.2 software (Philips). We aimed to replicate physiologically relevant circumferential and longitudinal displacement based on clinical values at ventricular midsection. Target midventricular displacements included 13.30 ± 0.66 mm (RV), 8.99 ± 0.49 mm (LV), and 7.15 ± 0.51 mm (septal longitudinal motion) [22].

B. Coronary Artery Flow Loop Setup

To simulate coronary flow, a peristaltic pump (INTLLAB, DP-520-460) was used to introduce fluid (distilled water) into the coronary arteries. The flow rate could be controlled between 170 and 460 mL/min. The pump motor was controlled via an Arduino Nano Every and a MOS driver module (IRF520 MOSFET). Clinically relevant pulsatile flow was created by varying the input voltage between two levels with a period of one second (60 bpm). Flow from the pump was synchronized with the intraventricular balloon inflation using the control box to ensure that the majority of coronary flow occurred during diastole, consistent with physiological conditions. The pressure inside the intraventricular balloon during inflation was measured using a pressure sensor (PRESS-S-000, PendoTECH), which was triggered in sync with the pump outflow. To direct flow into individual coronary arteries, a cannula (Vitalcor, Inc. 9/18 Fr. straight or 6.3/15 Fr. right-angle) was inserted into the coronary ostium of interest (either left or right).

The distal port of the cannula was connected to the outflow of the peristaltic pump via a combination of hose barb and Luer lock fittings. A custom 3D-printed plug adapter was used to secure the cannula in place within the coronary artery (**Fig. 3**). The plug, inserted into the aorta, contained an indentation for the cannula to fit snugly (≈ 2.25 mm diameter), with plug diameters (⌀) ranging from 2 to 2.5 cm to accommodate variations in heart and aorta size. Volumetric flow rate into the coronary arteries was measured using an ultrasonic flow probe (Transonic), connected to a T420 multichannel research console (Transonic Systems). Flow data was recorded using PowerLab (ADInstruments) and LabChart Pro version 8.1.16 software.

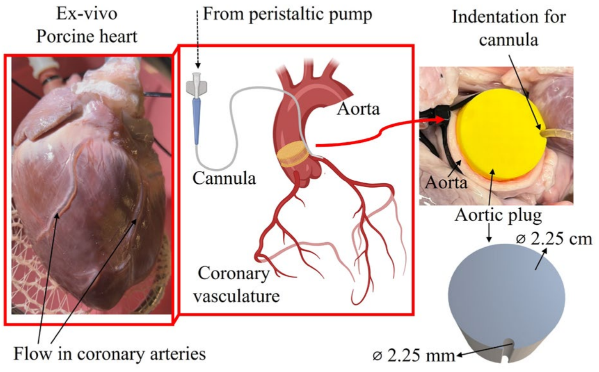

Fig. 3. Schematic and setup of the flow loop integration with coronary arteries. An aortic plug used to secure the cannula is also shown.

For convenience, the entire system (excluding the control box and peristaltic pump) was enclosed in a custom-built acrylic box (**Fig. 4**). This containment box included a tray to collect fluid drainage from the coronary flow, a fluid reservoir to supply fluid to the peristaltic pump inlet, and a metal rod with a ring stand to hold and support the heart at adjustable heights. This plug-and-play design enabled the system to be transferred from the research laboratory to the clinical catheterization laboratory.

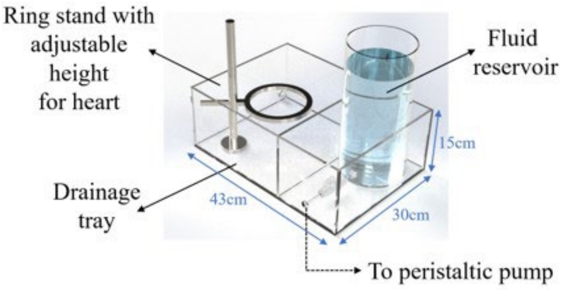

Fig. 4. Design of the custom-built acrylic housing setup.

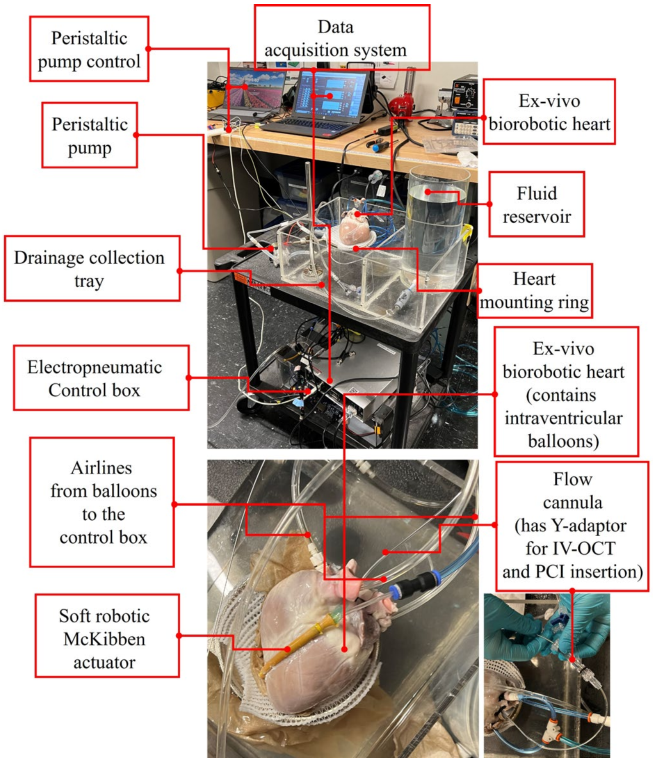

Fig. 5. Complete setup of the ex-vivo coronary artery simulator system. Data acquisition and fluid drainage systems are also shown.

C. Coronary artery imaging with Intravascular Optical Coherence Tomography (IV-OCT)

Imaging of the coronary arteries under healthy and diseased conditions was performed using a custom-built [23] IV-OCT system (100 frames/second) or a commercial system (LUNAWAVE, Terumo, 158 frames/second), both using commercially available 2.6 Fr FastView catheters (Terumo). Different flow rates were tested, and a pull-back procedure was performed to visualize the coronary vasculature, including bifurcations and branch points. A Y-connector was integrated into the flow loop at the distal end of the cannula to facilitate IV-OCT catheter insertion. One side of the Y-connector directed flow from the peristaltic pump into the coronary arteries, while the other arm with an integrated hemostasis valve allowed for the insertion of an IV-OCT catheter or a guidewire. The hemostasis valve adaptor attached to the end of the Y-connector ensures a fluid-tight seal around the IV-OCT probe, guidewire, or delivery system, maintaining the integrity of the flow during imaging and intervention. To simulate coronary artery dissection, a sharp guidewire was used to create two lumina within the coronary artery under pump flow, mimicking the pathology of SCAD. A coronary stent (Abbott GraftMaster RX Coronary Stent Graft: 3.5mm x 16mm) was implanted to repair the dissection. The placement and efficacy of the stent were confirmed using IV-OCT imaging.

The fully assembled ex-vivo coronary artery simulator is shown in **Fig. 5**, which demonstrates all critical components working together to replicate physiological conditions for coronary intervention testing.

III. RESULTS

A. Biomimetic Ventricular Wall Motion and Displacement

Ventricular wall motion was assessed using M-mode ultrasound imaging with two balloons in the RV and one in the LV, simulating physiological heartbeats at 60 bpm (**Fig. 6a**). The circumferential displacement of both the inner and outer ventricular walls at the midsection was measured at varying pressures (1-3 psi), with wall movement quantified in both ventricles (**Fig. 6b**, **Table 1**). The results showed that inner wall displacement was consistently larger than outer wall displacement in both the LV and RV. For the RV, circumferential displacement of the outer wall was measured at 11.14 ± 0.90 mm, while the inner wall reached 11.92 ± 1.10 mm at 1 psi. In comparison, clinically reported total clinically reported total displacement for the RV free wall ranges from 17.60 ± 0.82 mm at the base to 9.15 ± 0.30 mm at the apex, with 13.30 ± 0.66 mm for the midsection [22]. In the LV, the outer wall displacement at 1 psi was 9 mm, compared to 13.80 ± 1.30 mm for the inner wall at the same pressure. At higher pressures (2 psi), LV outer wall displacement increased to 9.80 ± 0.4 mm, while inner wall displacement reached 18.20 ± 0.45 mm. Clinically, total displacement in the LV free wall ranges from 11.61 ± 0.56 mm at the base to 6.24 ± 0.16 mm at the apex, with 8.99 ± 0.49 mm for the midsection [22]. In addition, localized longitudinal shortening near the left anterior descending artery (LAD) was created using the McKibben actuator, measured at the section represented by the red block in **Fig. 2**. Motion tracking revealed cyclical shortening during each cardiac cycle, with a peak longitudinal shortening of approximately 7 mm (or 0.7 cm) during systole (**Fig. 6c**, **Movie 1**). Clinically, longitudinal displacement in the septum region ranges from 9.03 ± 0.53 mm at the base to 3.83 ± 0.29 mm at the apex, with 7.15 ± 0.51 mm for the midsection. These findings reflect realistic longitudinal wall motion, highlighting the model's ability to replicate physiologically relevant circumferential and longitudinal myocardial motion in the region of interest. The displacement measurements align with the lower end of values reported in the literature. Further control and adjustment of wall displacement could be achieved by utilizing intraventricular balloons with larger volume capacities.

B. Coronary Flow Recapitulation

Coronary flow through the left anterior descending artery was assessed using an ultrasonic flow probe, color Doppler ultrasound, and pulsed-wave Doppler imaging. **Fig. 7a** shows the pulsatile volumetric flow rate (≈340 mL/min) in the LAD over time, demonstrating flow synchronized with the cardiac cycle. This observed flow rate is comparable to the reported values for healthy individuals, where the LAD flow rate is typically 228 ± 71 mL/min [24]. The high-frequency oscillations in the LAD coronary flow are caused by the peristaltic pump. Although the pump's input voltage was adjusted to simulate systolic and diastolic flow, the oscillations in flow are intrinsic to these pumps due to their mechanism of action using rollers. Using a pump with smoother flow dynamics, such as a piston-driven or diaphragm-based pulsatile system, could help minimize these fluctuations.

Color Doppler imaging further visualized the flow of blood inside the LAD, showing dynamic interaction between the coronary flow and the myocardial wall (**Fig. 7b**, **Movie 1**). This imaging confirmed the presence of continuous flow, synchronized with the simulated heartbeat.

Quantitative assessments using pulsed-wave Doppler (PW Doppler) revealed varying flow velocities across different conditions of rest within a peak flow velocity of approximately 20-45 cm/s, and higher peak velocities of increased stress (simulated hyperemia) of approximately 200 cm/s, and 400 cm/s, respectively (**Fig. 7c**, **Table 1**). Clinically, in healthy individuals at rest, the diastolic blood flow velocity in the LAD typically ranges between 10 to 40 cm/s, and during periods of increased demand, such as physical stress or pharmacologically induced hyperemia, the blood flow velocity can increase to 50 to 100 cm/s or higher [25, 26]. The velocities observed in our simulator are comparable to these physiological values, highlighting its ability to accurately replicate coronary flow profiles under both normal and hyperemic (stress) conditions.

Table 1. Comparison of measured values from the ex-vivo coronary artery simulator with reported physiological values [22, 24-26].

Parameter	Measured in simulator	Reported clinical values
RV Free Wall Displacement (Midsection)	11.14 ± 0.90 mm (Outer) / 11.92 ± 1.10 mm (Inner)	13.30 ± 0.66 mm
LV Free Wall Displacement (Midsection), 2 psi	9.80 ± 0.4 mm (Outer) / 18.20 ± 0.45 mm (Inner)	8.99 ± 0.49 mm
Septal Longitudinal Shortening (Midsection)	7 mm	7.15 ± 0.51 mm
LAD Flow Rate	~340 mL/min	228 ± 71 mL/min
LAD Flow Velocity (Rest)	20-45 cm/s	10-40 cm/s

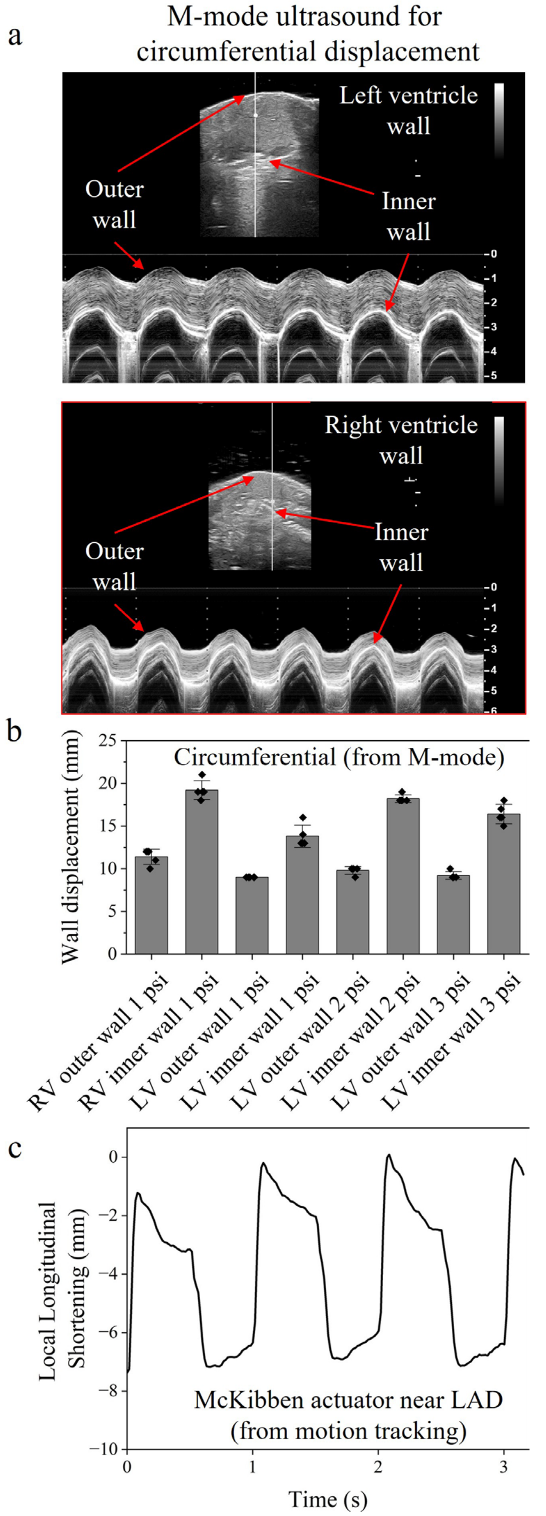

Fig. 6. (a) M-mode ultrasound images of the left ventricle (LV) and right ventricle (RV) walls, showing the circumferential displacement of the inner and outer ventricular walls during simulated heartbeats of 60 bpm. Note displacement here is shown in cm. (b) The bar plots represent summarized wall displacement values derived from the M-mode imaging, which provides a clear visual comparison of the data. The standard deviation is calculated from five consecutive beats to assess beat-to-beat variability. (c) Longitudinal shortening measured near the left anterior descending artery (LAD) using the McKibben actuator, captured through motion tracking over time. The steps in the measured displacement likely result from tracking the myocardial tissue, whose biomechanical response and nonlinear viscoelastic properties may cause localized strain distribution and relaxation effects.

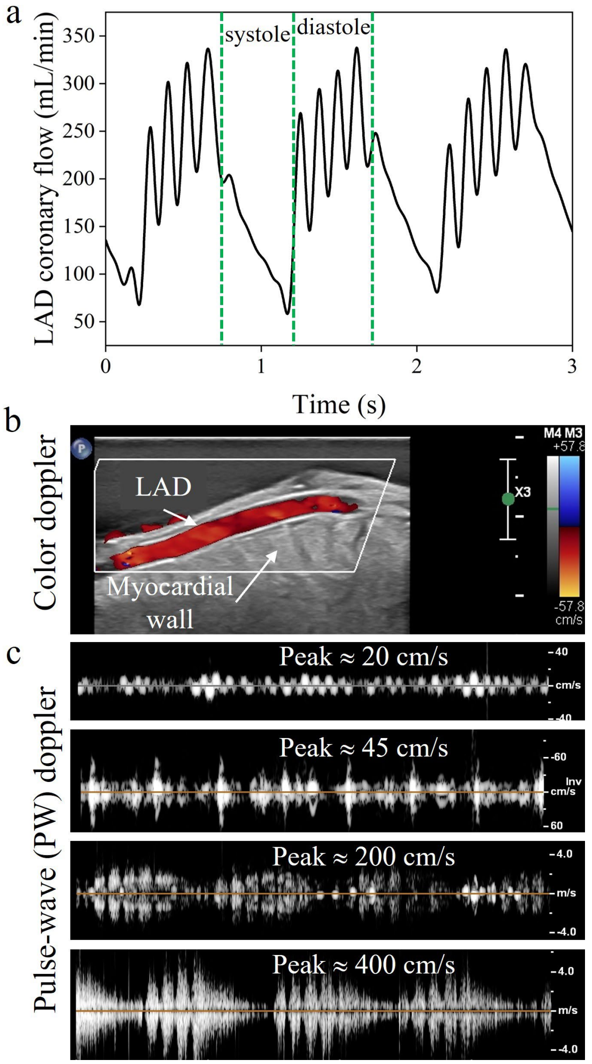

Fig. 7. (a) Left anterior descending artery (LAD) coronary flow rate (mL/min) over time, showing pulsatile flow synchronized with the simulated ventricular wall over a cardiac cycle. High-frequency peaks are caused by the peristaltic pump's rotational speed. (b) Color Doppler ultrasound image showing flow inside the LAD (c) Pulse-wave Doppler velocity waveforms show varying peak flow velocities.

C. *IV-OCT Imaging of Coronary Arteries*

IV-OCT was used to image the LAD coronary artery during simulated ventricular systole and diastole. The IV-OCT setup, illustrated in **Fig. 8a**, shows the catheter inserted into the coronary artery for high-resolution imaging. Cross-sectional OCT images captured during systole and diastole provided detailed visualization of the vessel wall. In **Fig. 8b**, the catheter is clearly visible inside the LAD, showing the anatomical differences between ventricular systole and diastole, where the vessel experiences cyclic contraction and expansion. Sequential pullback images captured along the length of the LAD during the pull-back procedure further identified key structural features, including bifurcations and variations in lumen size (**Movie 1**). **Fig. 8c** displays these sequential images, demonstrating how IV-OCT can accurately visualize complex coronary anatomy, including branching points, which are critical for assessing interventional strategies. The simulator enables the same high-resolution imaging used during PCI under realistic physiological conditions, providing valuable insights into coronary anatomy and dynamics during different phases of the cardiac cycle.

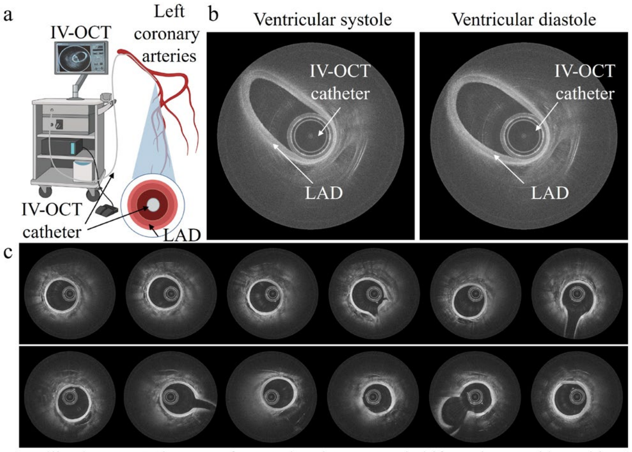

Pullback IV-OCT images of LAD showing anatomic bifurcations and branching

Fig. 8. Intravascular Optical Coherence Tomography (IV-OCT) imaging of the left anterior descending (LAD) coronary artery. (a) Diagram illustrates the IV-OCT setup with the catheter inserted into the coronary artery. (b) OCT cross-sectional images show the catheter inside the LAD, providing high-resolution views of the vessel wall during systole vs diastole. (c) Sequential cross-sectional images captured during the pull-back procedure.

D. Diseased Model of Coronary Dissection and Repair with Stent Deployment

A diseased model of SCAD was successfully recreated in the ex-vivo coronary artery simulator, demonstrating its ability to mimic pathological conditions. In this model, the dissection resulted in the formation of two distinct lumina within the LAD, simulating a clinical case where blood flow is divided between the true lumen and a false lumen formed by the dissection (**Fig. 9a**). IV-OCT imaging was used to visualize the dissection, capturing high-resolution cross-sectional images of the two-lumen channel. The imaging provided detailed views of the vessel, confirming the presence of a dissection with compromised flow (**Fig. 9b**). Following the creation of the dissection, a coronary stent was deployed using percutaneous coronary intervention techniques to restore vessel integrity. The IV-OCT images confirmed that the stent was deployed and expanded, consolidating the two-lumen dissection into a single functional lumen for blood flow (**Fig. 9c**). Quantitative analysis of the vessel diameter (**Fig. 9d**) showed that prior to stenting, the short-axis lumen diameter was measured at 0.9 mm during diastole and 0.6 mm during systole. After stent deployment, the lumen diameter increased to 1.7 mm in both systole and diastole, confirming successful expansion and restoration of vessel patency. During the pullback imaging following stent placement, it was observed that the proximal edge of the stent was poorly seated at another potential dissection site (**Movie 1**). IV-OCT imaging revealed an edge dissection at the proximal end of the stent, a complication that might have been difficult to detect using X-ray angiography alone. This finding emphasizes the value of intravascular imaging in detecting subtle post-implantation issues, especially for SCAD. Clinically, such an issue could be addressed by selecting a longer stent from the outset or by placing a second stent to overlap with the proximal edge. This is a clinically relevant finding, as poor stent apposition can lead to complications such as stent thrombosis, which can increase the risk of adverse patient outcomes. Detecting and addressing such issues during intervention is critical, and this observation highlights the value of the simulator to not only test and validate PCI techniques but also to provide critical insights into stent deployment outcomes and potential complications, further enhancing its utility for clinician training and research.

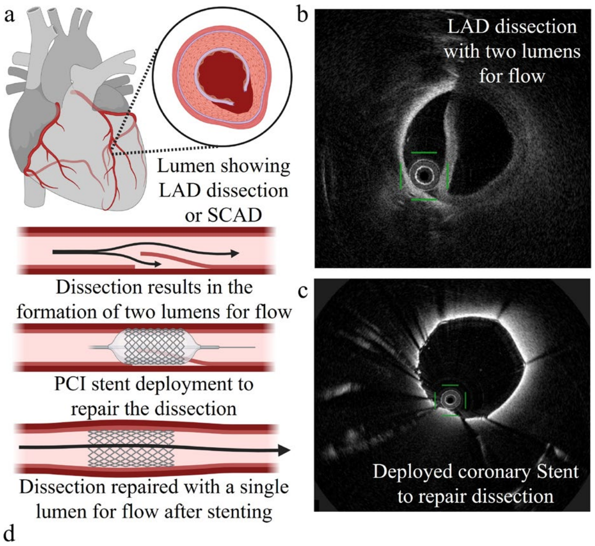

d

Condition	Short-axis diameter (systole)	Short-axis diameter (diastole)
Pre-stenting	0.6 mm	0.9 mm
Post-stenting	1.7 mm	1.7 mm

Fig. 9. (a) Schematic showing a left anterior descending (LAD) artery intimal dissection, resulting in a flap or dissected intimal section due to spontaneous coronary artery dissection (SCAD). The diagram illustrates the process of percutaneous coronary intervention (PCI) stent deployment to repair the dissection and restore a single lumen for flow. (b) IV-OCT cross-sectional images of the LAD dissection with two distinct lumina for flow. (c) Subsequent deployment of a coronary stent to repair the dissection. OCT confirms that the stent is fully expanded. (d) Vessel diameter before and after stenting, measured using the OCT catheter as a reference.

IV. CONCLUSION

We have developed a biorobotic benchtop ex-vivo coronary artery simulator that replicates physiological coronary flow and myocardial wall motion, providing a realistic platform for testing percutaneous coronary interventions, particularly in cases of SCAD. Designed to be compact and versatile, the system is well-suited for clinician training, education, and refinement of intervention techniques. Importantly, the simulator is fully compatible with IV-OCT, enabling highly detailed imaging of coronary arteries and intervention outcomes in real-time. This compatibility allows for clinically relevant testing, providing valuable insights into stent expansion, positioning, and potential complications like edge dissection, which may not be easily detectable with standard angiography. Our simulator is designed with portability in mind, addressing challenges associated with complex perfusion-based models. While explanted porcine hearts limit durability and transportability, the modular setup enables practical benchtop studies, such as transportation to a clinical catheterization lab. Creating lumina with a sharp guidewire requires precision but is feasible, as demonstrated by successful implementation without a surgical background, however user may need appropriate training for reproducibility. Our simulator replicates physiological coronary flow, indirectly reflecting pressure fluctuations during systole and diastole. While fluid pressure simulation is important, it is not explicitly controlled in the current model. Future iterations could incorporate pressure monitoring to enhance fidelity, especially for pressure-sensitive interventions. Future refinements will also aim to improve flow rate accuracy by replacing the peristaltic pump with a programmable pump synchronized with balloon actuation, better replicating physiological conditions. Future advancements, including the integration of calcification, atherosclerotic analogs, and vulnerable plaques into the coronary vessels, as well as 3D-printed femoral or radial insertion points and segments of the aorta, will further enhance the model for studying coronary atherosclerotic plaques and minimally invasive procedures. In the realm of percutaneous coronary interventions, this high-fidelity benchtop simulator could potentially also be used as a platform for validating computational models, as well as for functional design testing of stents, stent-grafts, balloons, and wires, enabling assessment of pulsatile flow interactions, positioning, deployment accuracy, sizing, and critical delivery parameters such as conformability, trackability, pushability, and torquability.

ACKNOWLEDGMENT

The authors would like to acknowledge the funding sources, including the National Institutes of Health (NIH R01EB033306, awarded to N.U-P. and E.T.R.) and the National Science Foundation (NSF grant number 1847541, awarded to E.T.R.) for this work. The illustrations were created with BioRender.com.

REFERENCES

[1] J. P. Duggan, A. S. Peters, G. D. Trachiotis, and J. L. Antevil, "Epidemiology of coronary artery disease," *Surgical Clinics,* vol. 102, no. 3, pp. 499-516, 2022.

[2] S. N. Hayes *et al.*, "Spontaneous coronary artery dissection: JACC state-of-the-art review," *Journal of the American College of Cardiology,* vol. 76, no. 8, pp. 961-984, 2020.

[3] S. N. Hayes *et al.*, "Spontaneous coronary artery dissection: current state of the science: a scientific statement from the American Heart Association," *Circulation,* vol. 137, no. 19, pp. e523-e557, 2018.

[4] S. Lee, C.-S. Kim, D. J. Oh, H. Yoo, and J. W. Kim, "Three-dimensional intravascular optical coherence tomography rendering assessment of spontaneous coronary artery dissection concomitant with left main ostial critical stenosis," *JACC: Cardiovascular Interventions,* vol. 7, no. 6, pp. e57-e59, 2014.

[5] C. J. Vrints, "Spontaneous coronary artery dissection," *Heart,* vol. 96, no. 10, pp. 801-808, 2010.

[6] D. Kotecha *et al.*, "Risks and benefits of percutaneous coronary intervention in spontaneous coronary artery dissection," *Heart,* vol. 107, no. 17, pp. 1398-1406, 2021.

[7] J. Lewey, S. C. El Hajj, and S. N. Hayes, "Spontaneous coronary artery dissection: new insights into this not-so-rare condition," *Annual Review of Medicine,* vol. 73, no. 1, pp. 339-354, 2022.

[8] T. Kariya, K. P. Yamada, O. Bikou, S. Tharakan, S. Miyashita, and K. Ishikawa, "Novel Porcine Model of Coronary Dissection Reveals the Impact of Impella on Dissected Coronary Arterial Hemodynamics," *Frontiers in Cardiovascular Medicine,* vol. 7, p. 162, 2020.

[9] A. R. Diéguez, B. C. Álvarez, A. Á. Carrillo, F. G. Peña, J. R. González-Juanatey, and R. T. Nouche, "A 3D printed patient-specific simulator for percutaneous coronary intervention," *Revista espanola de cardiologia (English ed.),* vol. 72, no. 5, pp. 424-426, 2019.

[10] Z. Sun, C. K. C. Ng, Y. H. Wong, and C. H. Yeong, "3D-printed coronary plaques to simulate high calcification in the coronary arteries for investigation of blooming artifacts," *Biomolecules,* vol. 11, no. 9, p. 1307, 2021.

[11] L. Rosalia *et al.*, "Soft robotic patient-specific hydrodynamic model of aortic stenosis and ventricular remodeling," *Science robotics,* vol. 8, no. 75, p. eade2184, 2023.

[12] C. Park, M. Singh, M. Y. Saeed, C. T. Nguyen, and E. T. Roche, "Biorobotic hybrid heart as a benchtop cardiac mitral valve simulator," *Device,* vol. 2, no. 1, 2024.

[13] F. J. Shahandashti, S. Asadian, N. Habibi, F. Gorjipour, A. Jalali, and Y. Toloueitabar, "Pulsatile versus non-pulsatile perfusion in coronary artery bypass operation: The comparison of laboratory and clinical outcomes," *Perfusion,* vol. 38, no. 5, pp. 1053-1061, Jul 2023, doi: 10.1177/02676591221096224.

[14] M. T. Vervoorn *et al.*, "A Cardioprotective perfusion protocol limits myocardial functional decline during ex situ heart perfusion," *JHLT Open,* vol. 3, p. 100042, 2024.

[15] M. Singh *et al.*, "Robotic right ventricle is a biohybrid platform that simulates right ventricular function in (patho)physiological conditions and intervention," *Nature Cardiovascular Research,* vol. 2, no. 12, pp. 1310-1326, 2023/12/01 2023, doi: 10.1038/s44161-023-00387-8.

[16] L. Hu *et al.*, "An implantable soft robotic ventilator augments inspiration in a pig model of respiratory insufficiency," *Nature Biomedical Engineering,* vol. 7, no. 2, pp. 110-123, 2023/02/01 2023, doi: 10.1038/s41551-022-00971-6.

[17] B. E. Bouma, M. Villiger, K. Otsuka, and W.-Y. Oh, "Intravascular optical coherence tomography," *Biomedical optics express,* vol. 8, no. 5, pp. 2660-2686, 2017.

[18] I.-K. Jang, G. Tearney, and B. Bouma, "Visualization of tissue prolapse between coronary stent struts by optical coherence tomography: comparison with intravascular ultrasound," *Circulation,* vol. 104, no. 22, pp. 2754-2754, 2001.

[19] C. Park, M. Singh, M. Y. Saeed, C. T. Nguyen, and E. T. Roche, "Biorobotic hybrid heart as a benchtop cardiac mitral valve simulator," *Device,* 2024.

[20] M. Singh *et al.*, "Robotic right ventricle is a biohybrid platform that simulates right ventricular function in (patho) physiological conditions and intervention," *Nature Cardiovascular Research,* pp. 1-17, 2023.

[21] M. Singh *et al.*, "Hemodynamic evaluation of biomaterial-based surgery for Tetralogy of Fallot using a biorobotic heart, in silico, and ovine models," *Science Translational Medicine,* vol. 16, no. 755, p. eadk2936, 2024, doi: doi:10.1126/scitranslmed.adk2936.

[22] I. Haber, D. N. Metaxas, T. Geva, and L. Axel, "Three-dimensional systolic kinematics of the right ventricle," *American Journal of Physiology-Heart and Circulatory Physiology,* vol. 289, no. 5, pp. H1826-H1833, 2005.

[23] M. Villiger *et al.*, "Repeatability assessment of intravascular polarimetry in patients," *IEEE transactions on medical imaging,* vol. 37, no. 7, pp. 1618-1625, 2018.

[24] S. Fournier *et al.*, "Normal values of thermodilution-derived absolute coronary blood flow and microvascular resistance in humans: Normal absolute coronary flow and resistance," *EuroIntervention,* vol. 17, no. 4, p. e309, 2021.

[25] M. A. Al-Mohaissen, "Echocardiographic assessment of primary microvascular angina and primary coronary microvascular dysfunction," *Trends in Cardiovascular Medicine,* vol. 33, no. 6, pp. 369-383, 2023.

[26] Y. Ueno, Y. Nakamura, H. Takashima, M. Kinoshita, and A. Soma, "Noninvasive assessment of coronary flow velocity and coronary flow velocity reserve in the right coronary artery by transthoracic Doppler echocardiography: comparison with intracoronary Doppler guidewire," *Journal of the American Society of Echocardiography,* vol. 15, no. 10, pp. 1074-1079, 2002.